New experimental evidences of corrugation formation due to rail longitudinal vibration mode

Zhang, Pan; Li, Zili

DOI
10.1080/23248378.2024.2336503

Publication date
2024

Document Version
Final published version

Published in
International Journal of Rail Transportation

International Journal of Rail Transportation

ISSN: (Print) (Online) Journal homepage: www.tandfonline.com/journals/tjrt20

New experimental evidences of corrugation formation due to rail longitudinal vibration mode

Pan Zhang & Zili Li

To cite this article: Pan Zhang & Zili Li (03 Apr 2024): New experimental evidences of corrugation formation due to rail longitudinal vibration mode, International Journal of Rail Transportation, DOI: 10.1080/23248378.2024.2336503

To link to this article: https://doi.org/10.1080/23248378.2024.2336503

Published online: 03 Apr 2024.

INTERNATIONAL JOURNAL OF RAIL TRANSPORTATION
https://doi.org/10.1080/23248378.2024.2336503

Taylor & Francis
Taylor & Francis Group

New experimental evidences of corrugation formation due to rail longitudinal vibration mode

Pan Zhang and Zili Li

Section of Railway Engineering, Delft University of Technology, Delft, The Netherlands

ABSTRACT

This paper aims at identifying the formation mechanism of short pitch rail corrugation using an improved configuration of a 1/5 scaled V-Track test rig. The loading conditions of the V-Track are designed to simulate the wheel-rail dynamic interactions on the tangent track. Corrugation initiation and consistent growth are successfully produced on the rail surface with a characteristic wavelength of about 6.0 mm, equivalent to the field one of 30 mm. By analysing the wheel-rail dynamic forces, the wheel and track dynamic behaviours across different rotations, it is found that the rail longitudinal vibration mode and its induced longitudinal dynamic force determine the corrugation formation with the necessary initial excitation.

ARTICLE HISTORY
Received 15 October 2023
Revised 24 March 2024
Accepted 26 March 2024

KEYWORDS
Short pitch corrugation; rail longitudinal vibration mode; initial excitation; differential wear

1. Introduction

Short pitch corrugation (hereinafter corrugation) refers to a type of (quasi-) periodic undulatory wear of rail surfaces on straight tracks or gentle curves according to the category in [1]. Its wavelength typically falls in a range of 20–80 mm [1]. One example of rail corrugation on the straight track of the Dutch railway network is shown in Figure 1, which is identified by shiny crests and dark valleys with a wavelength of approximately 40 mm. The short-wave corrugation in tight curves (e.g., in metro lines [2]) is also a severe problem in practice, which is not the focus of this research. The typical amplitude observed on the Dutch rail is about 30 μm. Rail corrugation can excite large wheel-rail contact forces, induce fierce vibration and noise, and accelerate track degradation. Therefore, it is important to identify the corrugation formation mechanism and develop the corresponding countermeasures.

Many hypotheses have been proposed in the literature to understand the corrugation formation process. The vertical pinned-pinned resonance has been widely recognized as the corrugation formation mechanism by many researchers, supported by numerical simulations and field measurements [3–7]. However, pinned-pinned resonance cannot easily explain the following field observations. First, corrugation does not occur everywhere on the rail with discrete supports where pinned-pinned resonance always exists [2]. Second, the single resonance frequency cannot explain the relative small variation of corrugation wavelength with the vehicle speed [1]. Third, corrugation has been reported on continuously supported rails where pinned-pinned resonance is absent [8]. Besides, the results in [9] indicate that the effect of pinned-pinned resonance on corrugation may be overestimated, and a 'resonance-free' mechanism considering longitudinal creepage was proposed to explain corrugation. Some researchers investigated the dynamic

CONTACT Zili Li z.li@tudelft.nl Section of Railway Engineering, Delft University of Technology, Stevinweg 1, Delft 2628 CN, The Netherlands

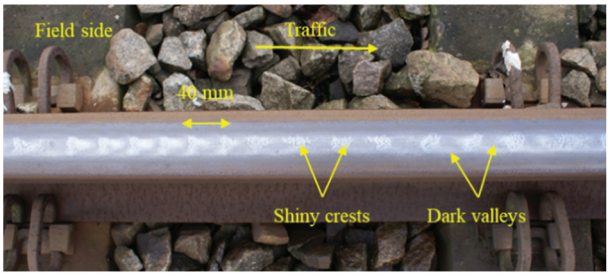

Figure 1. Short pitch rail corrugation observed on the straight track of the Dutch railway with a wavelength of approximately 40 mm.

resonance between multiple wheelset-rail interactions and found that the local rail vertical bending modes between the two wheelsets are responsible for corrugation formation [10,11]. The finite element (FE) simulation in [12–14] indicates that the friction-induced wheel-rail resonance leads to the periodic fluctuation of frictional power that causes rail corrugation. In [15,16], the influence of lateral track dynamics on corrugation formation is analysed combined with the vertical dynamics. Despite many theoretical studies being conducted on corrugation, there have been limited experimental validations of these theories with complete field data. One potential challenge is the acquisition of comprehensive long-term data in field tracks under controlled conditions to fully explain corrugation.

To overcome these limitations and ensure a more controlled and convenient environment, some laboratory facilities have been used to produce and understand corrugation [17–20]. The laboratory tests are a valuable intermediary step, allowing researchers to bridge the gap between theoretical models and practical field observations. A full-scale test rig was employed in [18] to study corrugation and reported that the high-frequency vibration of the test rig can initiate corrugation on the smooth contact surfaces of the wheel under specific test conditions. A downscale two-disk test rig was used to validate a tangent track corrugation model [20]. The test results show that the speed variation and the friction modifier can considerably reduce the corrugation growth rate. It should be noted that the majority of test apparatus mainly concentrate on the simulation of the wheel-rail contact of the vehicle-track interaction, with little consideration for accurately reproducing its high-frequency dynamic behaviours [21], which is crucial to the corrugation formation. Therefore, although corrugation was produced in these test facilities, their features and formation mechanism may not be comparable to those of the real vehicle-track system because of the dynamic dissimilarity.

Recently, new insight has been gained in [22–24] into the corrugation formation mechanism employing an advanced 3D finite element (FE) vehicle-track dynamic interaction model. Corrugation initiation and consistent growth have been successfully reproduced that share features similar to field corrugation. It is found that rail longitudinal vibration modes can be one mechanism initiating corrugation with the necessary initial excitation that allows flexibility for longitudinal vibration. Afterwards, an innovative downscale vehicle-track interaction test rig named 'V-Track' (see Figure 2) has been employed to perform a corrugation experiment to verify these insights [25]. Compared to other testing facilities, the V-Track has the advantage of simulating the high-frequency dynamic behaviours of the real vehicle-track system by the detailed treatment of wheel/rail material and geometry and the inclusion of important track structural components, such as fastenings and sleepers [21].

Although experimental evidence from the V-Track has been provided in [25] that verifies the new hypothesis of corrugation formation proposed in [23], there are still some limitations in the corrugation experiment. First, the lateral wheel-rail dynamic interaction is quite strong in the experiment due to a relatively large angle of attack (AoA), which is different from the FE simulation

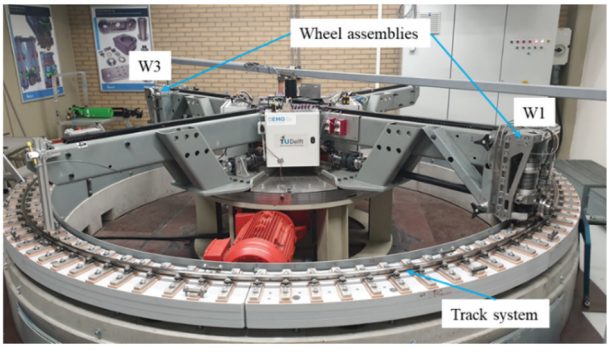

Figure 2. The downscale vehicle-track interaction test rig named V-Track for corrugation experiments. The V-Track consists of two wheel assemblies and a ring track system.

of a wheel rolling over the tangent track [23]. Better control of AoA and reduction of lateral dynamic force are thus needed. Second, the V-Track configuration in [25] utilized the standard S7 rails in the ring track for ease of construction, but their materials and profiles are not comparable to the real field rails. The scaled rails made of materials identical to the field rails are needed to more realistically study the wheel-rail dynamic contact and the resulting rail damage. Besides, the result of one corrugation experiment may not be sufficiently convincing for verification of [23] because of some potential randomness, and multiple experiments with similar testing conditions and approaches are necessary.

Therefore, in this paper, we further perform a corrugation experiment using an improved configuration of the V-Track test rig. The ring rails are cut from the real rail heads with a 1/5 scaled profile to ensure identical materials. The adjustment method of AoA is improved to reduce the lateral wheel-rail dynamic interaction. Overall, compared to [25], the current V-Track configuration achieves better similarity between the laboratory and the field, and its results are more comparable to the 3D FE simulations in [23]. Additionally, by combining the results of these two corrugation experiments, more insights are gained to better understand the corrugation formation mechanism. The paper is organized as follows. Section 2 introduces the experimental methodology of corrugation in the V-Track. Section 3 describes the corrugation consistent growth process of the rail surface. Section 4 identifies the corrugation formation mechanism by analysing the track dynamics and wheel-rail dynamic contact forces in three directions. Section 5 further discusses the experimental results to better understand corrugation. The main conclusions are drawn in Section 6.

2. Experimental methodology

In this section, the structure and components of the V-Track are briefly introduced. The corrugation experiment methodology is described, including the loading design, the input of initial excitation, and the data acquisition.

2.1. V-Track test rig

The current V-Track configuration consists of two wheel assemblies (W1 and W3 in short) running over a ring track system, see Figure 2. Figure 3(a) shows a close-up of the W1. Cylindrical wheels with a radius of 65 mm were used. The wheels were obtained from an actual wheel rim to ensure the material the same as in the field. Conical wheels will be used when studying the wheel-rail gauge contact [26,27]. The steel frame is driven by a motor called the 'driving motor' so that the wheel assemblies are pulled to run along the ring track. The maximum running speed is up to 40 km/h.

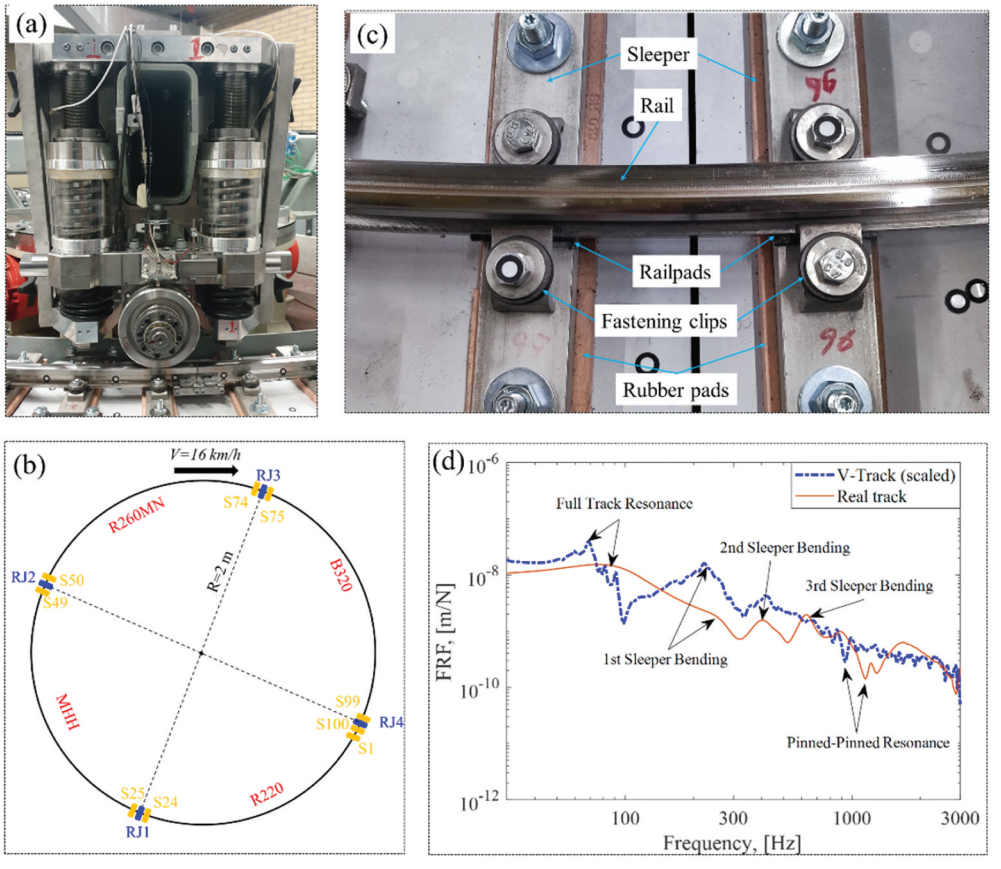

Figure 3. The wheel assembly and ring track system of the V-track. (a) The close-up of W1; (b) a schematic drawing of the ring track; (c) main track components; (d) comparison of the FRFs of the V-Track and the real vehicle-track system.

Another motor, called the 'braking motor,' is connected to the wheels through the braking shafts, which can apply a controllable negative/positive torque to the wheels to generate desired braking/traction forces. The AoA between the wheel and the rail is adjustable between −2° and + 2° and can be accurately measured by a digital gauge [28]. The vertical preload is adjustable using the preload springs in the range of 0–7500 N. A more detailed description of the V-Track wheel assembly can be found in [21,25].

The ring track system has a radius of 2 m, consisting of four sections of rails that are connected through four rail joints ('RJ' in short). A schematic drawing of the ring track is shown in Figure 3(b). Similar to the wheels, these rails were cut from the real rail heads to ensure identical materials. The four sections of rails were made of different materials, which are R220, MHH, R260MN, and B320, respectively, and their positions in the ring track can be seen in Figure 3(b). They have the same rail profile with a head curvature radius of 60 mm, approximately 1/5 scale of the UIC54 rail. The rails were fixed by fastenings on 100 evenly-distributed sleepers, with a sleeper distance of 125 mm, as shown in Figure 3(c). Each fastening consists of a railpad and a pair of clips that provide toe loads to the rail. The fastening clip includes six conical disc springs in series with a combined stiffness of 180 N/mm, which is approximately 1/5 of the real value (800 kN/m). The sleepers are numbered from 1 to 100 for positioning. For instance, S1 designates sleeper 1, and its position (see Figure 3(b)) is set as the starting point for data recording. The sleepers were supported on plywood layers with rubber pads in between. The rubber pads and plywood layers are used to simulate the elasticity of the track ballast and the subgrade, respectively. The parameters of the V-Track test rig are designed to be

Table 1. Values of parameters of the V-Track test rig and the real vehicle-track system in Dutch railway [4].

Components	Parameters	Values of V-Track	Values of Dutch Railway	Scale factor
Wheel and rail materials	Young's modulus	210 GPa	210 GPa	1
	Poisson's ratio	0.3	0.3	1
	Density	7800 kg/m^3	7800 kg/m^3	1
Wheel size	Radius	65 mm	345~460 mm	5~7
Rail size	Rail head radius	60 mm	300 mm	5
	Rail height	32 mm	159 mm	~5
Sleeper	Mass	1.2 kg	200 kg	~5^3
	Distance	125 mm	600 mm	~5
Primary suspension	Stiffness	230 kN/m	1.15 MN/m	5
	Damping	100 N.s/m	2500 N.s/m	5^2
Railpads	Stiffness	300 MN/m	1300 MN/m	~5
	Damping	2.0 kN.s/m	45 kN.s/m	~5^2
Rubber pads to simulate ballast	Stiffness	10 MN/m	45 MN/m	~5
	Damping	1.0 kN.s/m	32 kN.s/m	~5^2

approximately 1/5 scale of the real vehicle-track system in Dutch railway [4] based on the similarity law [21,25,29], as listed in Table 1.

To demonstrate the capability of the V-Track in representing real vehicle-track systems, we scaled the measured FRF on the V-Track at S11 (R220) according to the similarity law (frequency and magnitude scaled 1/5) and compared them to a typical track FRF in the Dutch railway [30], as shown in Figure 3(d). It can be seen that the V-Track represents well the general trend of FRF magnitudes of the real system. Furthermore, the V-Track successfully reproduces most of the track resonance modes of the real system at similar frequencies, for example, the full track resonance mode, the pinned-pinned resonance mode and the sleeper bending modes. Overall, the measured FRFs on the V-Track can well represent those of the real vehicle-track system, indicating good dynamic similarity.

2.2. Corrugation experiment

In this subsection, we introduce the loading conditions of the V-Track for the corrugation experiment, the initial excitation induced to the V-Track for corrugation initiation, and the data acquisition approach.

2.2.1. Loading design in the V-Track

Loads of the V-Track were designed to simulate the wheel-track dynamic interaction on the field tangent track for the corrugation experiment. The vertical (normal) load was designed to achieve a maximum contact pressure similar to the field. The AoA was designed to be as small as possible to simulate the wheel-rail lateral interaction on a tangent track. The braking motor was used to adjust one wheel torque (W1) that achieved an adhesion coefficient of around 0.1 and the other torque (W3) as small as possible, to simulate the driving and driven wheels, respectively, as shown in Figure 4(a). At a distance of 6.28 m, W1 and W3 had little interference with each other and did not represent two wheels in a bogie. The running speed was 16 km/h, which is the maximum safe speed in the current configuration without a safety cover on the wheel assembly. With the safety cover, a higher speed of up to 40 km/h can be applied, with which further tests will be performed in the future. The coefficient of friction (COF) is about 0.40 after cleaning and drying the rail and the wheel surfaces.

Figure 5(a–c) show the measured wheel-rail contact forces in the first rotation of the steel frame in the longitudinal, vertical and lateral directions after the final adjustment of the normal load, AoA and wheel torque (rotation 1). The contact forces are acquired with a sampling frequency of 16.67 kHz using a dynamometer (as shown in Figure 4(b)), which consists of four 3-component

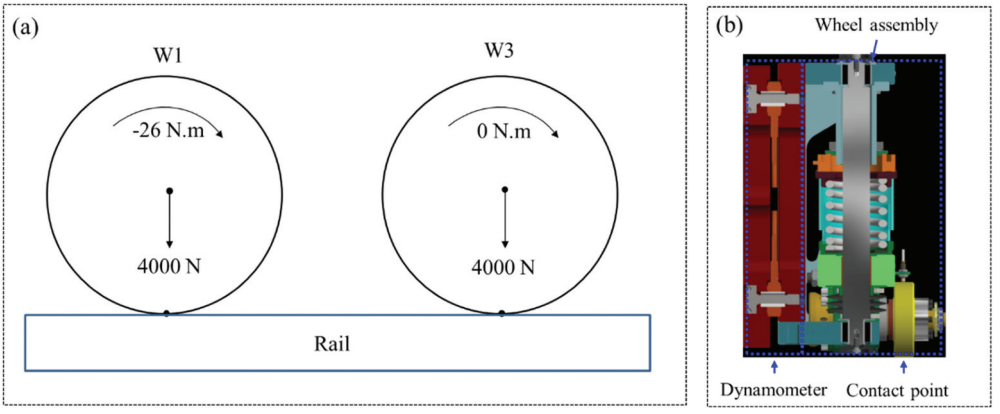

Figure 4. The designed loading conditions of the V-Track. (a) The schematic drawing of the loading conditions of W1 and W3; (b) the dynamometer for contact force measurement.

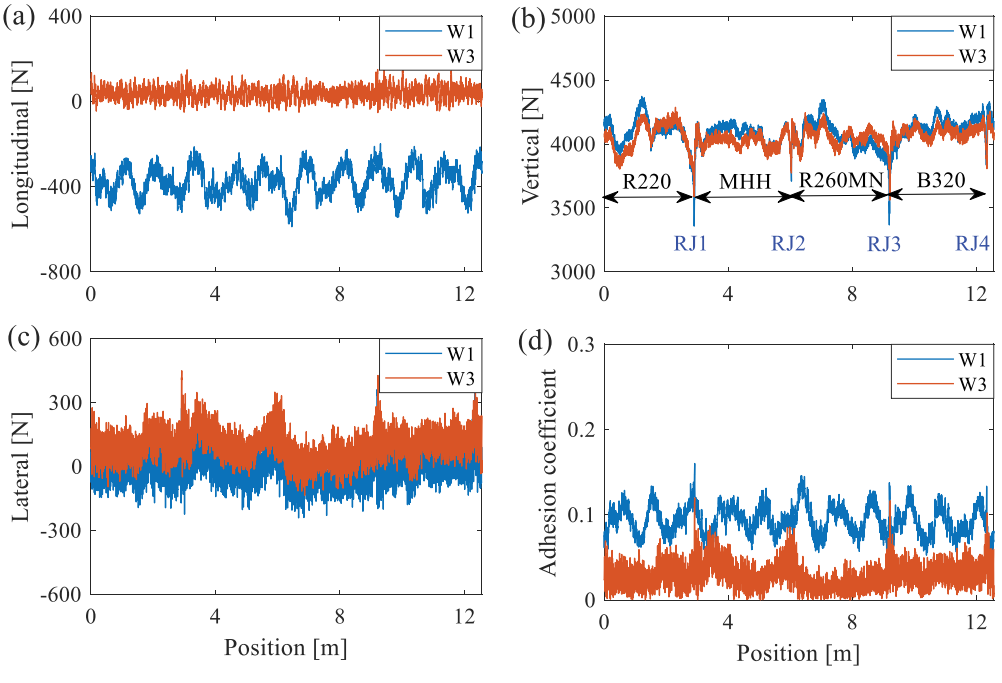

Figure 5. Loading conditions of W1 and W3 for corrugation experiment. (a) Longitudinal forces; (b) vertical forces; (c) lateral forces; (d) adhesion coefficient.

piezoelectric force sensors mounted between the wheel assembly and the steel frame [31]. The adhesion coefficient in Figure 5(d) was calculated as the quotient of the tangential force and the vertical (normal) force. As mentioned before, the starting (0 m) and ending (12.56 m) positions correspond to position S1.

Figure 4(b) shows that the vertical (normal) forces of W1 and W3 are close to and fluctuate around 4000 N, resulting in a maximum contact pressure of 1.35 Gpa. The four sharp peaks in this figure correspond to the positions of the four RJs, and in between are the vertical forces for the four rails, R220, MHH, R260MN, and B320, respectively. Compared to the previous corrugation experiment [25], the long-wave fluctuation has been significantly reduced and a more even vertical

force has been achieved along the ring track by a better adjustment of the vertical track irregularity. The average values of the lateral forces of W1 and W3 (see Figure 5(c)) are about −15 N and 90 N, respectively, corresponding to the considerably small AoAs. The longitudinal force of W1 (see Figure 5(a)) fluctuates around −400 N with an applied braking torque of −26 Nm. No wheel torque is applied to W3 so that the corresponding longitudinal force is close to 0 N. The average adhesion coefficients of W1 and W3 are about 0.1 and 0.03 respectively. Overall, the loads on the two wheel assemblies generally satisfy the designed loading conditions to simulate the wheel-track interaction on the tangent track.

2.2.2. Initial excitation for corrugation formation

In [23], the 3D FE simulations indicate that an initial excitation is necessary to induce the rail longitudinal vibration modes, generating fluctuation of longitudinal contact force, and causing differential wear and corrugation initiation. Such an initial excitation can be degraded fastenings modelled as a weak rail constraint.

In this corrugation experiment, some fastening clips were completely loosened without providing any toe loads to the rails to simulate the degraded fastenings, as shown in Figure 6(d). Specifically, the loose fastenings were on the rails made of R220 and R260MN for every other sleeper, and the fastenings on the three sleepers adjacent to the RJs were not loosened to avoid exaggerated impact that may damage the V-Track.

2.2.3. Data acquisition approach

During the corrugation experiment, the wheel-rail contact forces were continuously measured and recorded for each rotation. At every 2000 rotations, the V-Track was stopped for a visual inspection of the rail and wheel surfaces to check whether corrugation occurred or not. Meantime, the wear debris was cleaned to maintain a similar COF between the wheel and the rail throughout the entire

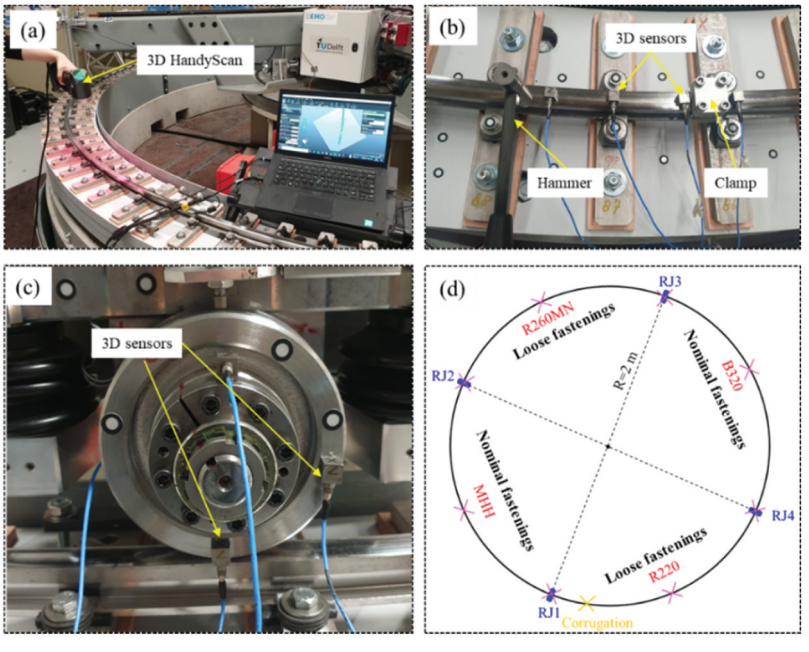

Figure 6. The experimental setups for data acquisition. (a) 3D HandyScan test; (b) hammer test on the track. The clamp is designed for the longitudinal excitation of the hammer; (c) hammer test on the wheel; the wheel was lifted without contact with the rail (d) test locations. Before corrugation was observed (16000 rotations), HandyScan and hammer tests were performed at eight locations (four joints and four middles at the four rails) for the health monitoring, as indicated by the pink crosses. After 16,000 rotations, the tests were performed at one more location where corrugation occurred, marked by the yellow cross.

experiment. 3D HandyScan tests (Figure 6(a)) were performed to measure the corrugation geometry. Hammer tests (Figure 6(b,c)) were performed to obtain the dynamic behaviours of the track and the wheels, which are related to the corrugation characteristic frequency and wavelength. The frequency response function (FRF) is calculated as follows [32].

$$H(f) = \frac{S_{aF}(f)}{S_{FF}(f)(2\pi f)^2} \tag{1}$$

where $H(f)$ is the FRF that is a complex-valued function; S_{aF} is the cross-spectrum between the acceleration a and the hammer force F; and S_{FF} is the auto-spectrum of the hammer force F. In this work, we mainly focus on analysing the magnitude of FRFs because their resonance peaks can be directly correlated to the characteristic frequencies of the dynamic contact forces and the corrugation. The analysis of the phases may also be interesting, which will be performed in the next-step work.

Before corrugation was observed (16000 rotations), 3D HandyScan and hammer tests were performed at eight locations (four joints and four middles at the four rails) for the health monitoring, as indicated by the pink crosses in Figure 6(d). S11 is one of the eight locations in the middle of the rail R220. After 16,000 rotations, the tests were performed at one more location where corrugation occurred on the R220 around S20, marked by the yellow cross in Figure 6(d).

3. Corrugation consistent growth in the V-Track

After 16,000 rotations, corrugation was first observed on the rail surface between S19 and S20 of the V-Track (from 2.26 m to 2.31 m), as shown in Figures 6(d) and 7. The fastening clips at S19 were loose and those at S20 were tight. The rail material is R220, the softest rail of the four rail sections. Afterwards, we run another 16,000 rotations to let the corrugation further grow. The 3D HandyScan tests were performed after 16,000, 22000 and 32,000 rotations, respectively, to record the corrugation growth.

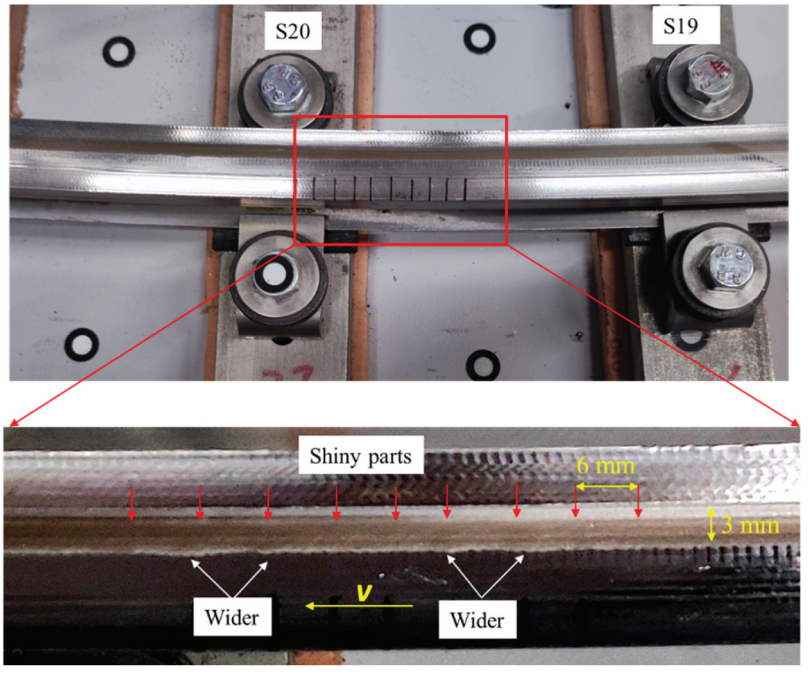

Figure 7. Reproduced corrugation on the rail R220 between S19 and S20 with a wavelength of about 6.0 mm.

In Figure 7, the locations of the corrugation marked by red arrows were shiny to the naked eye, although they looked like dark spots through the camera in this figure. Except for the colour contrast, we could also distinguish the corrugation by the relatively wider running band (marked by the white arrows) corresponding to the shiny parts. During the tests, the marked shiny parts of the corrugation barely change, indicating a consistent corrugation growth at a fixed location. The corrugation wavelength observed from this figure is approximately 6.0 mm. The running band is in the middle of the rail head with a width of about 3 mm, larger than the 2.3 mm calculated based on Hertz theory probably due to plastic deformation.

Figure 8 shows the corrugation geometry in the spatial domain after the 16,000, 22000, and 32,000 rotations. These results were measured by 3D HandyScan tests and obtained at the centre of the running band along the wheel running direction after bandpass filtering of 2–15 mm. Irregularities with wavelength shorter than 2 mm contributes insignificantly to the corrugation due to the contact filter, and with wavelength longer than 15 mm tend to obscure the corrugation growth trend due to their larger amplitudes. The measurement results of the initial rail roughness before starting the test (rotation 0) were not available in the corrugation zone, as explained in Figure 6(d). To gain insight into the initial rail roughness, we obtained the measurement data at S20 after 16,000 rotations that were at the same longitudinal locations as the corrugation, but 3 mm away from the centre line of the running band in the lateral direction. It is beyond the wheel-rail contact areas and represents the initial rail roughness resulting from the rail manufacturing process. Meanwhile, the roughness measurement data at S11 before starting the test are obtained along the longitudinal direction at two lateral positions. One lateral position is within the running band, and the other is 3 mm away from the running band. The roughness spectra of these three cases are close to each other, indicating that the initial rail roughness can be considered consistent along the rail. Therefore, the initial rail roughness outside the running band at S20 after 16,000 rotations can be approximately representative of those in the corrugation zone before starting the test, which was designated as rotation '0' and compared with the corrugation geometry in Figure 8. Besides, it is worth noting that the vertical shift of the curves at different rotations is not related to general wear or any physical changes during the test, but primarily intended for better visualization and comparison of the results.

The grey dashed lines in this figure correspond to the positions of the shiny parts in Figure 7. From the relatively deeper corrugation after 32,000 rotations, we can see that the shiny parts correspond to corrugation peaks. Using these nine lines as reference, the measured corrugation

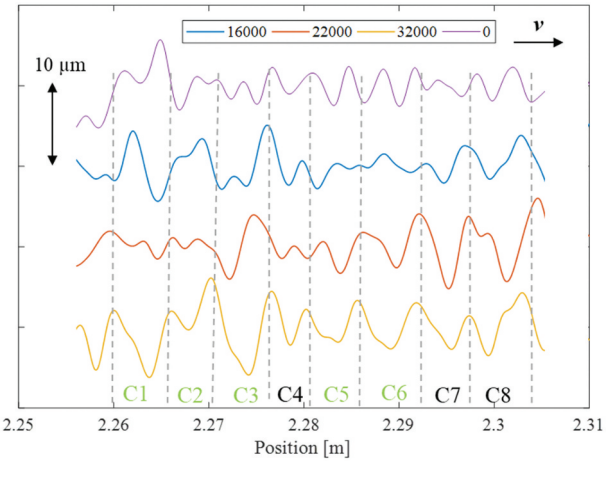

Figure 8. Measured corrugation geometry after the 16,000, 22000 and 32,000 rotations in the spatial domain from the 3D HandyScan tests. The result at '0' rotation corresponds to the initial rail roughness without wheel passages.

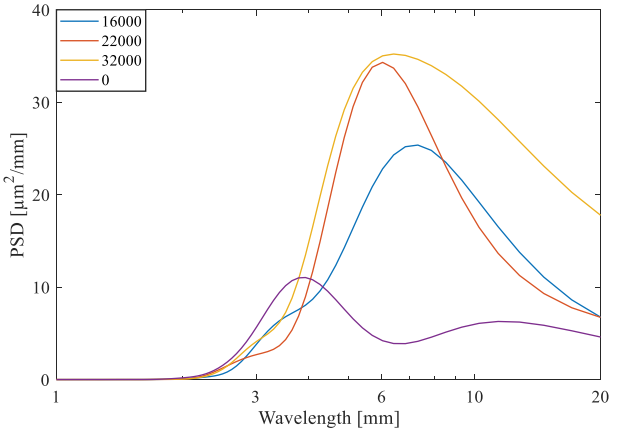

Figure 9. Reproduced corrugation geometry in the wavelength domain. The result at '0' rotation corresponds to the initial rail roughness without wheel passages.

was divided into eight waves from one corrugation peak to another, denoted by C1, C2, C8 with either black or green colour. If a wave after 16,000 rotations includes a complete cosinoidal shape, namely from a corrugation peak to a trough and then to a peak again, meantime its amplitude (from peak to trough) changes insignificantly compared to that after 32,000 rotations, this wave is set to be black, indicating it barely grows. Otherwise, it is set to be green to indicate a growing wave.

We can see from Figure 8 that C1, C2, C3, C5, and C6 are in green, and they considerably grow from 16,000 to 32,000 rotations with different growth trends. Specifically, C1, C2, and C6 show a peak instead of a trough at the middle of the waves after 16,000 rotations; these peaks are probably from the initial rail roughness and worn off after 22,000 rotations, then become troughs after 32,000 rotations. For C3 and C5, the corrugation amplitude significantly increases. Compared to C1, C2, C3, C5, and C6, the waves C4, C7 and C8 do not grow much from 16,000 rotations to 32,000 rotations, and thus are in black.

Two findings are summarized from the growth trend of these corrugation waves from Figure 8. First, the wear of the rail surface that causes the corrugation is differential. Second, the differential wear has a constant wavelength and phase so that the wear accumulates and the corrugation consistently grows at a fixed location. In addition, it can be seen that the initial rail roughness at '0' rotation does not exhibit a correlation with the observed corrugation in terms of the spatial distribution.

Figure 9 shows the measured corrugation geometry in the wavelength domain. It can be seen that the relatively deeper corrugation after 22,000 and 32,000 rotations has a major wavelength component of about 6 mm, approximately equivalent to 30 mm of field corrugation wavelengths considering a scale factor of 1/5, falling in the short pitch range (20–80 mm). The initial corrugation wavelength after 16,000 rotations is about 7.0 mm. The initial rail roughness at '0' rotation exhibits a predominant peak at 4.0 mm and a less pronounced peak at 11.4 mm. The valley at 6.4 mm between these two peaks confirms that corrugation does not exist on the initial rail surface, but is caused by the wheel-track dynamic interaction and the resulting differential wear. Besides, it is found that the overall magnitude of rail profile decrease from 0 to 32,000 rotations for wavelengths smaller than 4.0 mm, probably influenced by the contact filter effect. In contrast, for larger wavelength, the magnitude considerably increases, with the highest growth rate observed at the corrugation wavelength of 6.0 mm.

4. Corrugation formation mechanism

In this section, the corrugation formation mechanism is analysed according to the measured wheel-rail dynamic contact forces, track dynamics and wheel dynamics.

4.1. The longitudinal dynamic force dominates corrugation formation

Wheel-rail dynamic contact forces, which cause differential wear on the rail surfaces, determine the corrugation formation. Figure 10 shows the measured wheel-rail contact forces of W1 and W3 in the longitudinal, vertical and lateral directions in the first rotation (rotation 1). The pink dashed boxes mark the position of the reproduced corrugation, i.e., from 2.26 m to 2.31 m.

We first focus on the four tangential (frictional) contact force components that cause the differential wear and thus corrugation, namely the longitudinal and lateral forces of W1 and W3. It can be seen that the average magnitude of the longitudinal force of W1 in the corrugation zone is about 400 N, much larger than those of the other three components which are below 100 N. This significant difference in magnitudes implies that the longitudinal force of W1 contributes the most to the friction power and is thus dominant for rail wear, which is the corrugation damage mechanism. Assuming that the fluctuation of the other three components can cause corrugation and is inconsistent with that of the longitudinal force of W1, the corrugation caused by the three other components will probably be worn out and cannot grow. Therefore, it can be concluded that the longitudinal force of W1 is dominant for the wear of the rail surface and thus corrugation formation. The vertical (normal) forces of W1 and W3 in the corrugation zone have an average value of about 4150 N.

It is also observed from Figure 10 that all the six contact force components show relatively strong fluctuation around their average magnitude in the corrugation zone. This dynamic fluctuation determines the wavelength-fixing mechanism of corrugation [1]. To identify the corrugation

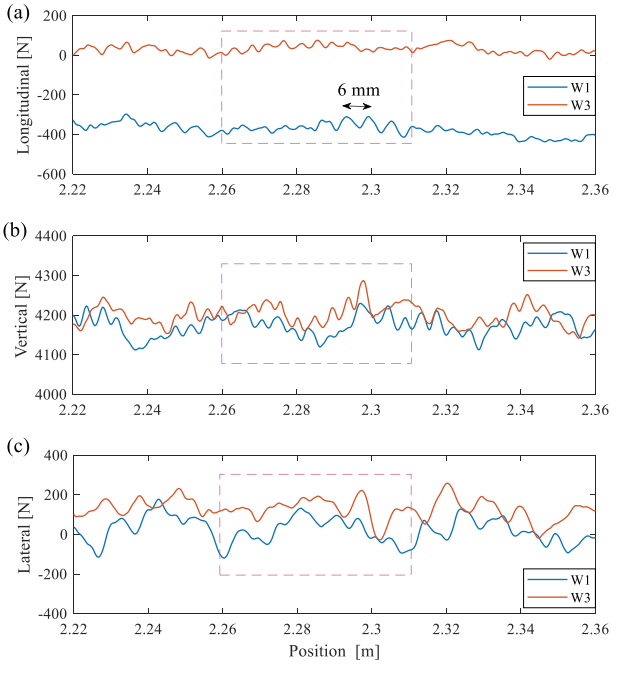

Figure 10. Measured wheel-rail dynamic contact forces of W1 and W3 in the spatial domain at rotation 1. (a) Longitudinal forces; (b) vertical forces; (c) lateral forces. The pink dashed boxes mark the corrugation zone.

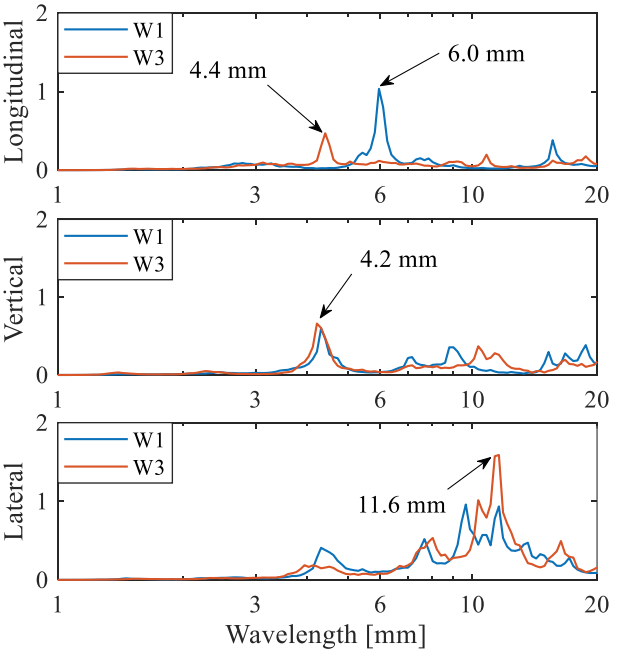

Figure 11. Wheel-rail dynamic contact forces of W1 and W3 in the wavelength domain in the corrugation zone at rotation 1.

formation mechanism, the contact forces in the wavelength domain are obtained in the corrugation zone, as shown in Figure 11.

It can be seen that the longitudinal force of W1 has a major wavelength component of 6.0 mm, corresponding well to the characteristic wavelength of the corrugation. The longitudinal force of W3 has a major wavelength of about 4.4 mm, the vertical forces of W1 and W3 about 4.2 mm, and the lateral forces of W1 and W3 about 11.6 mm. Their major wavelength components are quite far away from the corrugation wavelength and thus not responsible for the corrugation development. Nevertheless, they will contribute to the overall rail roughness growth in the wavelength range from 4.0 mm to 20.0 mm, as shown in Figure 9. Meanwhile, it is worth noting that the wavelengths/frequencies of the tangential forces (longitudinal and lateral forces) are not necessarily the same as those of the normal (vertical) force in the unsaturated condition.

In summary, the longitudinal force of W1 has the largest average magnitude and thus dominates the rail wear, which is the damage mechanism of corrugation. Meanwhile, its major wavelength component matches precisely with the corrugation characteristic wavelength. Therefore, it is concluded that the longitudinal dynamic force of W1 is dominant for the corrugation formation. This conclusion aligns with the finding in [33] that at higher frequency, and with equal amplitudes of imposed relative displacement, the longitudinal force exceeds the vertical force by an appreciable factor.

4.2. Rail longitudinal vibration mode determines the corrugation frequency and wavelength

It is reported that all types of corrugation that have been documented to date are essentially constant-frequency phenomena [34], and the eigen frequencies of the vehicle-track system determine the corrugation frequencies [23]. The characteristic frequency f can be calculated by dividing the running speed v with a characteristic wavelength λ, as follows.

$$f = \frac{v}{\lambda} \tag{2}$$

With a running speed of 16 km/h, the characteristic frequency of the corrugation is calculated as 741 Hz, corresponding to the wavelength component of 6.0 mm. To better understand the corrugation formation mechanism, the wheel-rail dynamic forces are analysed in the time-frequency domains employing the synchro-squeezed wavelet transform [35], as shown in Figure 12. It can be seen that the longitudinal force of W1 has a major frequency component of 760 Hz, corresponding well to the characteristic frequency of the corrugation. The longitudinal force of W3 has a major wavelength of about 1020 Hz, the vertical forces of W1 and W3 about 1050 Hz, and the lateral forces of W1 and W3 about 400 Hz. Their major frequency components are quite far away from the corrugation frequency and thus not responsible for the corrugation development. It is worth noting from Figure 12(a) that the overall vibration energy at around 760 Hz is relatively stronger in the corrugation zone compared to the non-corrugation zone. Furthermore, Figure 12 shows that the characteristic frequencies of the dynamic forces vary with distance, probably caused by the local variation of the track dynamics [36] and track irregularities.

Dynamic behaviours of the track and the W1 characterized by FRFs were derived from the hammer tests after 16,000 rotations. Figures 13(a–c) show the measured FRFs in the longitudinal, vertical and lateral directions, with the excitations at S19.5 (the middle between S19 and S20) and S20. The resonance peaks and anti-resonance valleys correspond to different rail vibration modes [37,38]. Figure 13(d) shows the measured FRFs with both radial and axial excitations. The radial direction is mainly relevant to longitudinal and vertical wheel-rail dynamic interactions, while the axial direction relates to lateral interaction. The predominant peaks at 2430 Hz and 4660 Hz correspond to the wheel modes of zero nodal circle and one nodal diameter, and zero nodal circle and two nodal diameters, respectively. It is found that the corrugation frequency of 741 Hz corresponds well to a rail longitudinal vibration mode at around 750 Hz, and does not correlate to the vertical and lateral vibration modes and the wheel modes, as indicated by the pink dashed lines. It is thus concluded that rail longitudinal vibration mode determines the corrugation characteristic frequency and wavelength.

Combining the measurement results of corrugation geometry (Figures 7 and 8), wheel-rail dynamic contact forces (Figures 9 and 10) and wheel and track dynamic behaviours (Figure 13),

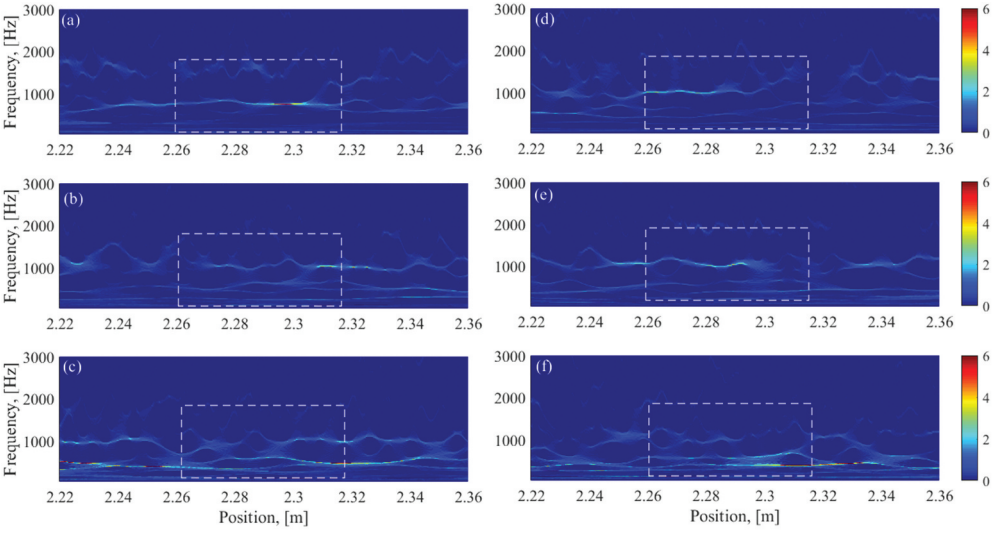

Figure 12. Measured wheel-rail dynamic contact forces of W1 and W3 in the spatial-frequency domains at rotation 1. The white dashed boxes mark the corrugation zone.

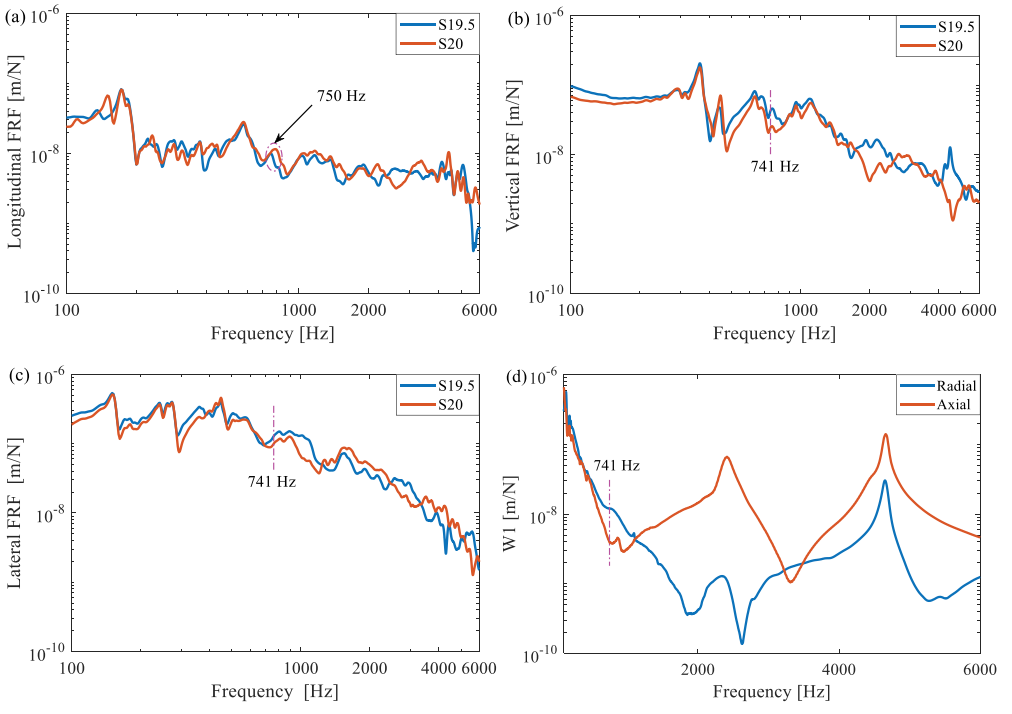

Figure 13. Measured FRFs of the track and W1 after 16,000 rotations. FRFs of the track with the excitations at S19.5 (the middle of S19 and S20) and S20 in the (a) longitudinal; (b) vertical; and (c) lateral directions; (d) FRFs of W1 with both radial and axial excitations. The dashed lines in (b), (c) and (d) mark the corrugation characteristic frequency.

the corrugation formation mechanism is identified. First, the loose fastening clips of the rail R220 serve as the initial excitation to the wheel-track system of the V-Track, causing a weak longitudinal constraint to the rail that releases the longitudinal vibration mode at 750 Hz. When the wheel rolls over the rail with a speed of 16 km/h, this vibration mode is excited and induces longitudinal dynamic contact force with a wavelength of about 6.0 mm. This dynamic force then causes differential wear of the rail surface and finally the corrugation initiation and consistent growth. In summary, the rail longitudinal vibration mode and its induced longitudinal dynamic force determine the corrugation formation in the V-Track.

4.3. Contact forces and dynamics of wheel-track system during corrugation development

To further understand the corrugation development mechanism, the measured wheel-rail contact forces with W1 at rotations 1, 16,000, 22000 and 32,000 are shown in the spatial (Figure 14) and wavelength (Figure 15) domains, respectively. Besides, the dynamic behaviours of the track with corrugation and W1 after rotations 16000, 22000 and 32,000 rotations are also presented in Figure 16.

It can be seen from Figures 14(a) and 15(a) that the longitudinal dynamic force with W1 generally shows a consistent wavelength and phase. The dominant wavelength component of about 6.0 mm is observed at rotations 1, 16,000 and 32,000, aligning well with the corrugation wavelength. This result confirms the conclusion that the longitudinal dynamic force plays a dominant role in corrugation development. Besides, it is found that a slight shift in wavelength occurs from 6.0 mm to 6.5 mm at rotations 16,000 and 22,000, which can be attributed to the longer initial corrugation wavelength of 7.0 mm measured at rotations 16000, as depicted in Figure 9. This

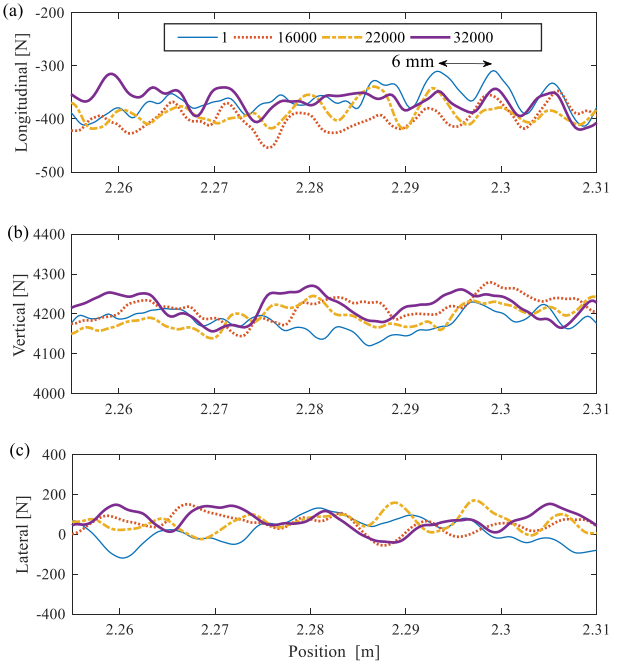

Figure 14. Measured wheel-rail contact forces with W1 at rotations 1, 16000, 22000 and 32,000 in the (a) longitudinal; (b) vertical; (c) lateral directions in the corrugation zone.

longer wavelength may be a consequence of wavelength modulation caused by the 6.0 mm longitudinal force and the 8.1 mm lateral force (see Figure 15(c)) during the corrugation initiation stage.

Figure 14(b) and 15(b) show that the vertical dynamic force overall exhibits less consistency across the different rotations when compared to the longitudinal force. Except for a wavelength component at 4.2 mm, we can observe from Figure 15(b) another major wavelength component at 16.7 mm, which is contributed to the rail roughness growth at longer wavelengths (see Figure 9). Besides, it is found from Figures 15(b,c) that at rotation 32,000, the vertical and lateral forces have a wavelength component at about 6.0 mm despite a relatively small magnitude. This wavelength component is not observed at rotation 1, which should be a results of the excitation by the rail corrugation. The possible reason for the relatively small magnitude is that no resonance modes are found at the corrugation frequency in the vertical and lateral directions (see Figure 13). Furthermore, the relatively low running speed (16 km/h) and small amplitude of corrugation (i.e., 10 um) may result in the small forced vibration energy.

Figure 14(c) illustrates that the lateral force appears to follow a random pattern across the different rotations in the spatial domain in terms of the wavelength and phase. This can possibly be attributed to the relatively small average magnitude of the lateral force (below 100 N) due to a small AoA, making it more susceptible to random factors. Besides, the rail and wheel profile wear may cause slight changes of the wheel-rail contact positions, contributing to the inconsistency of the lateral force across different rotations, as well as those of the longitudinal and vertical forces. Figure 15(c) indicates that the lateral force has relatively larger magnitude at around 4.4 mm and within the range between 7.0 mm and 15.0 mm, which is contributed to the rail roughness development within the corresponding wavelength range.

Figure 16 shows that FRFs of the track at S20 and W1 closely align with each other after rotations 16,000, 22000 and 32,000, indicating the dynamic behaviours of the track and the wheel barely change during the tests. The variation of contact forces across different rotations in Figures 12 and 13 should be primarily related to the alterations at the wheel-rail interface. The relatively large

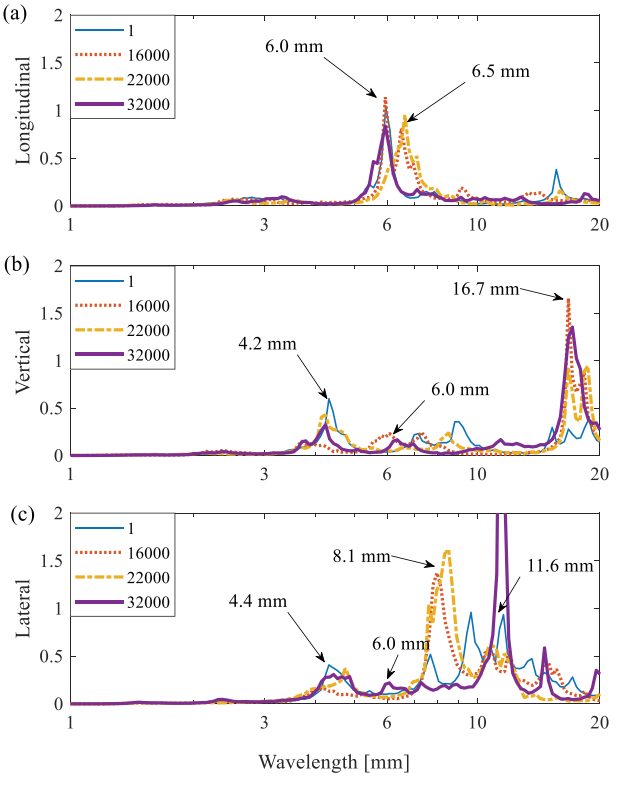

Figure 15. Measured wheel-rail contact forces with W1 in the wavelength domain at rotations 1, 16000, 22000 and 32,000 in the (a) longitudinal; (b) vertical; (c) lateral directions in the corrugation zone.

deviation in the wheel FRFs is a result of slight shifts in the hammer impact locations, which were challenging to control precisely on a cylindrical wheel surface.

Based on the aforementioned data and analysis, the evolution of the rail surface roughness and corrugation becomes evident. The initial rail roughness exhibits a predominant peak at 4.0 mm, a less pronounced peak at 11.4 mm, and a valley at around 6.4 mm. Afterwards, during the test, the longitudinal dynamic force of W1 is dominant for rail roughness growth within the wavelength range of 5.0–7.0 mm, particularly at the corrugation wavelength of around 6.0 mm. The vertical dynamic force increases the rail roughness in both longer wavelength range of 15.0–20.0 mm and the shorter wavelength of around 4.0–5.0 mm. The lateral dynamic force mainly contributes to the rail roughness growth in the wavelength range of 7.0–15.0 mm, and has influences in the 4.0–5.0 mm range. Among these forces, the longitudinal force of W1 plays a predominant role in rail wear and has the highest consistency in wavelengths and phases across the different rotations, hence leading to the dominant rail roughness growth in the range of 5.0–7.0 mm and the development of rail corrugation at around 6.0 mm.

5. Discussion

In this section, we further discuss the experimental results in the V-Track and compare them with the literature to better understand corrugation.

5.1. *Verification of corrugation formation mechanism in* [23]

Recently, Z. Li *et al.* [23] proposed a new hypothesis for the corrugation formation process, based on simulations employing a 3D FE wheel-track dynamic interaction model. The simulation results

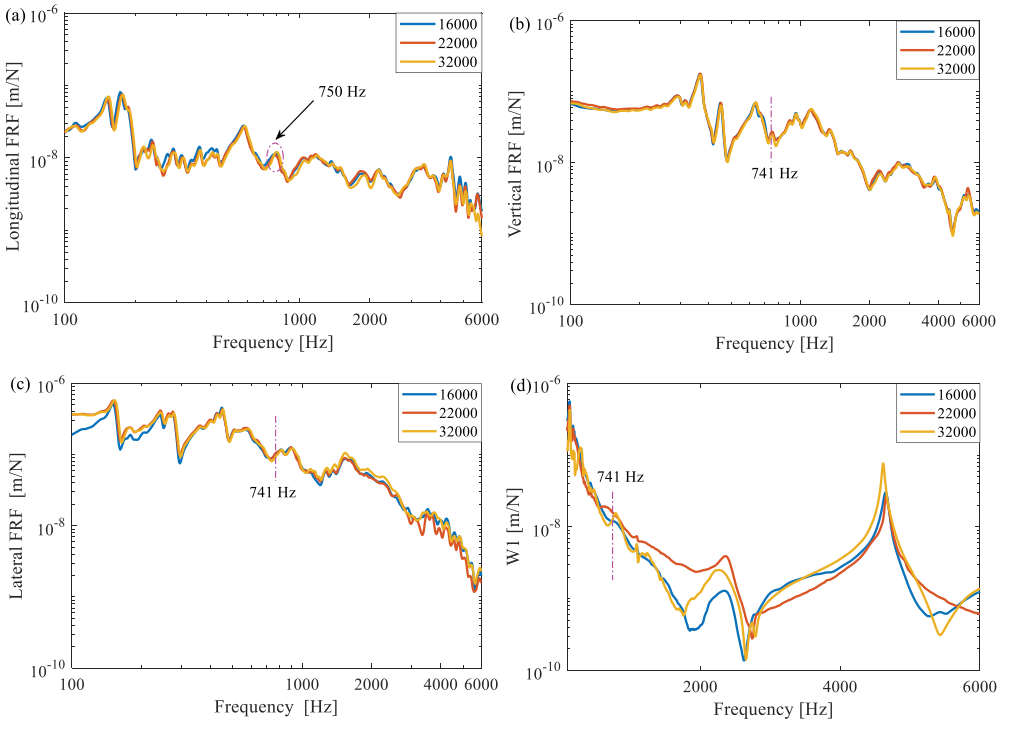

Figure 16. Measured FRFs of the track and W1 after 16,000, 22000 and 32,000 rotations. Track FRFs were obtained with the excitations at S20 in the (a) longitudinal; (b) vertical; and (c) lateral directions; (d) W1 FRFs with radial excitation. The dashed lines in (b), (c) and (d) mark the corrugation characteristic frequency.

indicate that rail longitudinal vibration modes, instead of the commonly considered vertical modes, are dominant for corrugation initiation, when with effective initiation excitation. This hypothesis has been experimentally verified on another configuration of the V-Track [25]. However, as introduced in Section 1, there are some limitations of the corrugation experiment in [25]. One major limitation is the strong wheel-rail lateral dynamic interaction due to a relatively large AoA in the experiment, which is different from the FE simulation condition in [23]. The resulting lateral dynamic force also contributes to the corrugation development together with the longitudinal one, making the formation mechanism partly different from that proposed in [23].

In the current configuration of the V-Track, we improve the control method of the AoA with a digital gauge [28] and considerably reduce the lateral contact force. Therefore, the wheel-rail dynamic interaction is more comparable to the numerical simulation in [23] of a wheel rolling over on a tangent track. The experimental results better verify the simulation results that the rail longitudinal vibration mode and its induced longitudinal force are dominant for corrugation formation by excluding the effect of lateral vibration modes and lateral dynamic force.

5.2. Comparison with the produced corrugation in [25]

The standard S7 rails used in [25] have cross-section geometry and materials different from the rails used in the current V-Track configuration. Corrugation is successfully produced on both types of rails, with the necessary initial excitation from the loose fastenings. This phenomenon agrees with the field observation that corrugation happens to different rail profiles and grades [8]. It may thus be inferred that corrugation can develop on various rails as long as the differential wear is induced by the longitudinal rail vibration modes under the wheel-rail frictional rolling contact. In addition, the successful reproduction of corrugation on two separate tests with a similar formation

mechanism has demonstrated the reproductivity and reliability of the corrugation experiment using the V-Track test rig.

Meanwhile, it is noted that corrugation amplitude (maximum peak to trough distance) reaches up to 60 μm after 10,500 rotations in [25], which is only 10 μm after 32,000 rotations in the current experiment (see Figure 8). Corrugation in [22] propagates over a longer rail of about five sleeper spans. The corrugation in [25] is much severer and grows much faster. The corrugation severity is probably determined by the intensity of the initial excitation. In [25], the fastening clips were installed only by every four sleepers, while by every other sleeper in the current experiment. The significantly weaker fastening constraints in [25] correspond to the greater intensity of the initial excitation to the wheel-track system, causing larger fluctuation amplitude of the longitudinal dynamic force and more differential wear, and thus severer corrugation. The larger corrugation growth rate in [25] could be also related to the smaller hardness of the S7 rail (170 HB).

In [25], the major corrugation wavelength is 6.4 mm with a running speed of 13 km/h. In the current experiment, the running speed increases by 23% to 16 km/h, while the corrugation wavelength is 6.0 mm and barely changes (−6%). The insensitive variation of corrugation wavelength to the traffic speed in the V-Track agrees with the field observation [1]. According to the corrugation formation mechanism [18], it is found that the wheel-track system selects to resonate at the rail longitudinal mode of 574 Hz with a speed of 13 km/h, and 750 Hz with 16 km/h. The different triggered frequencies in these two tests could be related to different rail fastening constraint methods. This result indicates that corrugation initiates essentially by frequency selection instead of wavelength selection, agreeing with the numerical analysis in [23]. More corrugation experiments with different running speeds will be performed in future work to verify this.

5.3. The necessity of effective initial excitation for corrugation formation

In the experiment, corrugation was only observed on R220 and not on the other three rails. According to the numerical analysis in [23], a necessary condition for corrugation formation is an effective initiation excitation that allows flexibility for longitudinal resonance. Figure 17 shows the longitudinal FRFs of the four rails R220 (S20), MHH (S36), R260MN (S60) and B320 (S86). They achieve a general similarity in the overall frequency range of 100–6000 Hz, indicating a certain level of reproducibility of track dynamics in the V-track test rig. It can be seen that the rail vibration mode corresponding to the corrugation frequency (indicated by the green oval) is released only for R220 due to the loose fastenings.

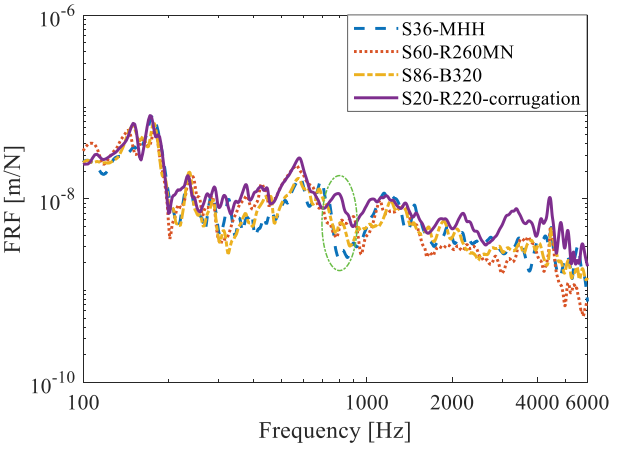

Figure 17. Measured longitudinal FRFs of the four rails R220 (S20), MHH (S36), R260MN (S60) and B320 (S86). The green circle marks the frequency range near the corrugation frequency.

Although the fastenings were also loosened for R260MN to serve as the initial excitation, the rail longitudinal modes that can effectively induce corrugation initiation are not excited. This result indicates the variation of the track dynamics in different sections of the rail in the V-Track test rig, the same nature as the track variability along the rails in field conditions. A possible reason is that the remaining fastening clips on R260MN are tighter than those on R220 because of some manual errors, which provide stronger rail longitudinal constraints. It is thus inferred that the intensity of the initial excitation should be large enough to effectively excite rail longitudinal vibration modes for corrugation initiation. Besides, it is noted that wheel-rail longitudinal resonance for corrugation formation only occurs at 741 Hz, not at other rail longitudinal modes such as at 150, 580 or 1170 Hz. This frequency selection may be related to the wheel-rail contact characteristics and the wheel speed, similar to the 'contact filter' effect that will mitigate the wheel-rail resonance in a certain wavelength range. In future work, we will further analyse the reason behind this observation with the help of numerical simulation.

5.4. The influence of the wheel torque on the longitudinal dynamic force

Based on the previous analysis in Section 4, it is concluded that the longitudinal dynamic force of W1 is dominant for the corrugation formation at 6.0 mm, and it is induced by the wheel-rail resonance at the rail longitudinal vibration mode at about 750 Hz with a speed of 16 km/h. One may argue that the longitudinal dynamic force may also originate from the wheel control system, which can be examined by looking at, i.e., the torque applied and measured on the wheel based on the following equation.

$$F = M/r \tag{3}$$

where F is the longitudinal force, M is the wheel torque, and r is the wheel radius which is 65 mm.

In the corrugation experiment, we controlled the torque on W1 by setting a nominal value of −26 Nm to achieve an adhesion coefficient of about 0.1. Besides, we ensured that no torque (0 Nm) was applied to W3 by dismantling the braking shaft associated with it. The actual torques applied to W1 and W3 during the test were measured using torque sensors, as shown in Figure 18(a). It can be seen that the actual wheel torques fluctuate around their respective nominal values of −26 Nm and 0 Nm. Their nominal values correspond well to the quasi-static (average) values of wheel-rail longitudinal forces (−400 N of W1 and 0 N of W3 as depicted in Figure 10) based on Equation (3).

However, in terms of the dynamic characteristics, Figure 18(b) reveals that the measured torque of W1 has two major wavelength components at 8.5 mm and 16.7 mm, and exhibits no relations to those of the longitudinal dynamic force of W1 (see Figure 11) and corrugation wavelength at 6.0 mm. These wavelength components may be related to the natural frequencies

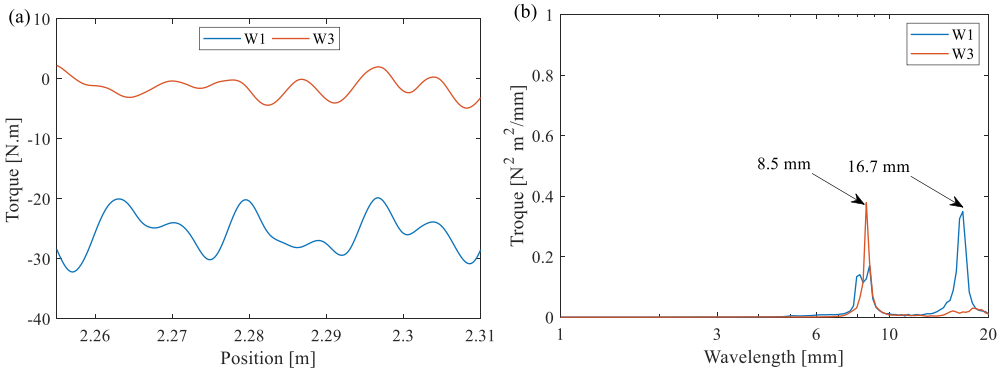

Figure 18. Measured torques of W1 and W3 at rotation 1 in the corrugation zone in the (a) spatial; and (b) wavelength domains.

of the braking motor and the associated components, and these fluctuations are isolated from the wheel assemblies transmitted through the braking shafts. Therefore, it is concluded that the fluctuation of the applied wheel torque influences little on the longitudinal dynamic force and the corrugation formation.

6. Conclusions

In this paper, we performed an experimental investigation on short pitch corrugation using an improved configuration of the V-Track test rig. The V-Track consists of two wheel assemblies (W1 and W3) and four ring rails that are made of materials identical to the field wheel and rail with a 1/5 scaled profile. The loading conditions of the V-Track were designed to simulate the wheel-track dynamic interaction on the field tangent track. Corrugation was successfully produced on the R220 rail between S19 and S20. Its spatial distribution and wavelength component were captured by the 3D HandyScan test. Based on the measurement results of wheel-rail contact forces and the wheel and track dynamic behaviours across different rotations, the corrugation formation mechanism was identified. The main conclusions are summarized as follows.

(1) The rail corrugation has been reproduced in the V-Track with a characteristic wavelength of 6.0 mm.
(2) The observation and measurement data indicate that rail corrugation consistently grows at a fixed location with the continuous accumulation of differential wear.
(3) Rail longitudinal vibration mode and its induced longitudinal wheel-rail dynamic force determine the corrugation formation when with the necessary initial excitation.
(4) The loose fastenings can serve as effective initial excitation to cause corrugation.
(5) The intensity of initial excitation to the wheel-track system influences the corrugation formation, growth rate and severity.
(6) The wheel resonance modes and the fluctuation of the wheel torques have insignificant influence on the corrugation formation.

Overall, this work contributes to a better understanding of the corrugation formation mechanism. Considering the dynamic similarity between the V-Track and the field railway, the results obtained from the V-Track test rig are valuable to provide insights into the corrugation formation mechanism in the field. In future work, field tests and monitoring need to be conducted to complement and validate the findings obtained from laboratory experiments. Besides, a numerical simulation of the corrugation formation in the V-Track will be performed to link the scaled laboratory tests to the full-scale reality. More tests with different running speeds will be conducted to identify the relationship between the corrugation wavelength and traffic speed. The corrugation mitigation approach proposed in [39] will be validated in the V-Track. More quantitative comparisons between the V-Track test rig and real railway system will be performed to further demonstrate their dynamic similarity, which will better bridge the gap between the laboratory and field tests.

Acknowledgements

The authors thank Jan Moraal for performing the V-Track tests and acquiring the data. The authors thank Julian He, Gokul Jayasree Krishnan, Siwarak Unsiwilai, Fang Ren and Chen Shen for helping with the 3D HandyScan test, hammer test, and hardness test. The authors thank Alfredo Núñez for his constructive feedback to improve this paper.

Disclosure statement

No potential conflict of interest was reported by the author(s).

References

[1] Grassie S, Kalousek J. Rail corrugation: characteristics, causes and treatments. Proc Inst Mech Eng, Part F: J Rail and Rapid Transit. 1993;207:57–68.

[2] Mei G, Chen G. Slip of wheels on rails: the root cause for rail undulant wear. Wear. 2023;523:204727. doi: 10.1016/j.wear.2023.204727

[3] Hempelmann K, Knothe K. An extended linear model for the prediction of short pitch corrugation. Wear. 1996;191(1–2):161–169. doi: 10.1016/0043-1648(95)06747-7

[4] Hiensch M, Nielsen JC, Verheijen E. Rail corrugation in the Netherlands—measurements and simulations. Wear. 2002;253(1–2):140–149. doi: 10.1016/S0043-1648(02)00093-5

[5] Nielsen J. Numerical prediction of rail roughness growth on tangent railway tracks. J Sound Vib. 2003;267(3):537–548. doi: 10.1016/S0022-460X(03)00713-2

[6] Grassie SL. Short wavelength rail corrugation: field trials and measuring technology. Wear. 1996;191(1–2):149–160. doi: 10.1016/0043-1648(95)06755-8

[7] Bosso N, Magelli M, Zampieri N. Simulation of wheel and rail profile wear: a review of numerical models. Rail Eng Sci. 2022;30(4):403–436. doi: 10.1007/s40534-022-00279-w

[8] Oostermeijer K. Review on short pitch rail corrugation studies. Wear. 2008;265(9–10):1231–1237. doi: 10.1016/j.wear.2008.01.037

[9] Afferrante L, Ciavarella M. Short-pitch rail corrugation: a possible resonance-free regime as a step forward to explain the "enigma"? Wear. 2009;266(9–10):934–944. doi: 10.1016/j.wear.2008.12.003

[10] Wu T, Thompson D. An investigation into rail corrugation due to micro-slip under multiple wheel/rail interactions. Wear. 2005;258(7–8):1115–1125. doi: 10.1016/j.wear.2004.03.060

[11] Ma C, Gao L, Xin T, et al. The dynamic resonance under multiple flexible wheelset-rail interactions and its influence on rail corrugation for high-speed railway. J Sound Vib. 2021;498:115968. doi: 10.1016/j.jsv.2021.115968

[12] Liu X, Tang Y, Wang P, et al. Forming process model of rail corrugation based on friction induced torsional vibration determined by vertical dynamics. Wear. 2022;502-503:204396. doi: 10.1016/j.wear.2022.204396

[13] Cui X, He Z, Huang B, et al. Study on the effects of wheel-rail friction self-excited vibration and feedback vibration of corrugated irregularity on rail corrugation. Wear. 2021;477:203854. doi: 10.1016/j.wear.2021.203854

[14] Chen GX, Cui XL, Qian WJ. Investigation into rail corrugation in high-speed railway tracks from the viewpoint of the frictional self-excited vibration of a wheel–rail system. J Mod Transp. 2016;24(2):124–131. doi: 10.1007/s40534-016-0106-6

[15] Muller S. A linear wheel–track model to predict instability and short pitch corrugation. J Sound Vibr. 1999;227(5):899–913. doi: 10.1006/jsvi.1999.2981

[16] Robles R, Correa N, Vadillo EG, et al. Comprehensive efficient vertical and lateral track dynamic model to study the evolution of rail corrugation in sharp curves. J Sound Vibr. 2023;545:117448. doi: 10.1016/j.jsv.2022.117448

[17] Suda Y, Komine H, Iwasa T, et al. Experimental study on mechanism of rail corrugation using corrugation simulator. Wear. 2002;253(1–2):162–171. doi: 10.1016/S0043-1648(02)00095-9

[18] Jin X, Wen Z Rail corrugation formation studied with a full-scale test facility and numerical analysis. Proc Inst Mech Eng, Part F: J Eng Tribol. 2007;221:675–698.

[19] Saulot A, Descartes S, Berthier Y. Sharp curved track corrugation: from corrugation observed on-site, to corrugation reproduced on simulators. Tribol Int. 2009;42(11–12):1691–1705. doi: 10.1016/j.triboint.2009.04.042

[20] Bellette P, Meehan P, Daniel W. Validation of a tangent track corrugation model with a two disk test rig. Wear. 2011;271(1–2):268–277. doi: 10.1016/j.wear.2010.10.020

[21] Naeimi M, Li Z, Petrov RH, et al. Development of a new downscale setup for wheel-rail contact experiments under impact loading conditions. Exp Tech. 2018;42(1):1–17. doi: 10.1007/s40799-017-0216-z

[22] Li S, Li Z, Núñez A, et al. New insights into the short pitch corrugation enigma based on 3D-FE coupled dynamic vehicle-track modeling of frictional rolling contact. Appl Sci. 2017;7(8):807. doi: 10.3390/app7080807

[23] Li Z, Li S, Zhang P, et al. Mechanism of short pitch rail corrugation: initial excitation and frequency selection for consistent initiation and growth. Int J Rail Trans. 2022;12(1):1–36. doi: 10.1080/23248378.2022.2156402

[24] Zhang P, Li S, Dollevoet R, et al. Parametric investigation of railway fastenings into the formation and mitigation of short pitch corrugation. Rail Eng Sci. 2024. doi: 10.1007/s40534-024-00332-w

[25] Zhang P, Li Z. Experimental study on the development mechanism of short pitch corrugation using a downscale V-Track test rig. Tribol Int. 2023;180:108293. doi: 10.1016/j.triboint.2023.108293

[26] Ren F, Yang Z, Hajizad O, et al. Experimental investigation into the initiation of head check damage using V-Track. 12th International Conference on Contact Mechanics and Wear of Rail/Wheel Systems; 2022 Sep 4–7; Melbourne, VIC, Australia. 2022.

[27] Qian Y, Wang P, Xie K, et al. Development and application of a calculation method for the equivalent conicity in high-speed turnout zones. Veh Syst Dyn. 2022;60(1):96–113. doi: 10.1080/00423114.2020.1802046
[28] Yang Z, Zhang P, Moraal J, et al. An experimental study on the effects of friction modifiers on wheel–rail dynamic interactions with various angles of attack. Rail Eng Sci. 2022;30(3):360–382. doi: 10.1007/s40534-022-00285-y
[29] Jaschinski A, Chollet H, Iwnicki S, et al. The application of roller rigs to railway vehicle dynamics. Veh Syst Dyn. 1999;31(5–6):345–392. doi: 10.1076/vesd.31.5.345.8360
[30] Shen C, Dollevoet R, Li Z. Fast and robust identification of railway track stiffness from simple field measurement. Mech Syst Signal Process. 2021;152:107431. doi: 10.1016/j.ymssp.2020.107431
[31] Zhang P, Moraal J, Li Z. Design, calibration and validation of a wheel-rail contact force measurement system in V-Track. Measurement. 2021;175:109105. doi: 10.1016/j.measurement.2021.109105
[32] Avitabile P. Experimental modal analysis. Sound Vib. 2001;35:20–31.
[33] Grassie S, Gregory R, Johnson K. The dynamic response of railway track to high frequency longitudinal excitation. J Mech Eng Sci. 1982;24(2):97–102. doi: 10.1243/JMES_JOUR_1982_024_018_02
[34] Grassie S Rail corrugation: characteristics, causes, and treatments. Proc Inst Mech Eng, Part F: J Rail and Rapid Transit. 2009;223:581–596.
[35] Shen C, Zhang P, Dollevoet R, et al. Evaluating railway track stiffness using axle box accelerations: a digital twin approach. Mech Syst Signal Process. 2023;204:110730. doi: 10.1016/j.ymssp.2023.110730
[36] Shen C, Deng X, Wei Z, et al. Comparisons between beam and continuum models for modelling wheel-rail impact at a singular rail surface defect. Int J Mech Sci. 2021;198:106400. doi: 10.1016/j.ijmecsci.2021.106400
[37] Zhang P, Li S, Núñez A, et al. Multimodal dispersive waves in a free rail: numerical modeling and experimental investigation. Mech Syst Signal Process. 2021;150:107305. doi: 10.1016/j.ymssp.2020.107305
[38] Zhang P, Li S, Núñez A, et al. Vibration modes and wave propagation of the rail under fastening constraint. Mech Syst Signal Process. 2021;160:107933. doi: 10.1016/j.ymssp.2021.107933
[39] Zhang P, Li S, Li Z. Short pitch corrugation mitigation by rail constraint design. Int J Mech Sci. 2022;243:108037. doi: 10.1016/j.ijmecsci.2022.108037